Analysis of Barrier Scattering with Real and Complex Quantum Trajectories[†]

Brad A. Rowland* and Robert E. Wyatt

Institute for Theoretical Chemistry and Department of Chemistry and Biochemistry, The University of Texas at Austin, 1 University Station A5300, Austin, Texas 78712

Received: March 28, 2007; In Final Form: May 24, 2007

In this study, an analysis of the one-dimensional Eckart and Gaussian barrier scattering problems is undertaken using approximate quantum trajectories. Individual quantum trajectories are computed using the derivative propagation method (DPM). Both real-valued and complex-valued DPM quantum trajectories are employed. Of interest are the deep tunneling and the higher energy barrier scattering problems in cases in which the scattering barrier is "thick" by comparison to the width of the initial wave packet. For higher energy scattering problems, it is found that real-valued DPM trajectories very accurately reproduce the transmitted probability densities at low orders when compared to large fixed-grid calculations. However, higher orders must be introduced to obtain good probabilities for deep tunneling problems. Complex-valued DPM is found to accurately reproduce transmitted probability densities at low order for both the deep tunneling and the higher energy scattering problems. Of particular note, complex-classical trajectories are found to very nearly give the exact result for the deep barrier tunneling scattering problem, and the complex DPM converges well at high orders for these thick barrier scattering problems. A variety of analyses are performed to elucidate the dynamics of complex-valued DPM trajectories. The complex-extended barrier potentials are examined in detail, including an analysis of the complex force. Of particular interest are initial conditions for complex-valued DPM trajectories known as isochrones. All trajectories launched from an isochrone arrive on the real axis on the transmitted side of the barrier at the same time. The computation and properties of isochrones as well as the behavior of the initial wave packet in the complex plane are also examined.

1. Introduction

Quantum wave packet dynamics can provide considerable insight into problems of interest in chemical physics such as photodissociation, barrier scattering, and femtochemical processes.[1] Traditionally, quantum wave packet dynamics calculations involved the solution of the time-dependent Schrödinger equation (TDSE) through the use of fixed grids or basis set expansions. Recently, much work has been focused upon the development and application of nonlocal quantum trajectory methods to these problems.[2]

In 1952, David Bohm[3,4] provided a formulation that gave deterministic quantum trajectories but at the expense of a nonlocal, state-dependent quantum potential. This was based on a much earlier pilot wave formulation of quantum mechanics as provided by Madelung[5] and de Broglie.[6] Holland[7,8] has provided much interpretation and analysis of quantum hydrodynamics. Alternatively, the quantum hydrodynamic equations of motion can be obtained through a momentum-moment expansion of the Wigner function in phase space. This work is based upon early studies conducted by Takabaysi.[9] Bughardt and Cederbaum formulated quantum hydrodynamic equations of motion for mixed (and pure) states[10] as well as for coupled electronic states.[11] This formulation has been extended to dissipative systems.[12]

The first viable computational approach to quantum trajectory dynamics, the quantum trajectory method (QTM), was introduced by Lopreore and Wyatt[13] in 1999. The QTM propagates quantum wave packets through the use of a correleated ensemble of Lagrangian trajectories (i.e., the grid points travel along at the velocity of the probability fluid). The QTM requires the use of function fitting (i.e., moving weighted least squares) to evaluate the quantum potential at each update. The QTM was extended to barrier scattering;[14] however, the QTM has stability issues when nodes form in the evolving wave packet. Babyuk and Wyatt worked on addressing the node problem[15,16] and extending QTM to multidimensional reactive scattering problems.[17−19]

There has been recent work on extending quantum trajectories to problems with many degrees of freedom. Kendrick[20] used arbitrary Lagrangian−Eulerian trajectories and artificial viscosity to stabilize the propagating wave packet in barrier scattering processes. This work was subsequently extended to two-dimensional problems by Pauler and Kendrick[21] and eventually to multidimensional problems as well.[22] Poirier and co-workers have also done much work on the bipolar decomposition of the wave function in the reconciliation of semiclassical dynamics with Bohmian dynamics.[23−25] Rassolov and Garashchuk[26] have introduced an approximate linearized quantum potential into the hydrodynamic equations of motion. This served to stabilize the wave function around nodes. Even greater stability was obtained by introducing a mixed polar-coordinate space representation of the wave function.[27] This was successfully extended to nonadiabatic systems.[28]

The derivative propagation method (DPM) was developed by Trahan, Hughes, and Wyatt[29] as an alternative way to solve the quantum hydrodynamic equations by propagating individual quantum trajectories (as opposed to the ensemble required by QTM). QTM is an exact formulation of the quantum hydrody-

---

* Author to whom correspondence should be addressed. Phone: (512) 471-0238. E-mail: browland@mail.utexas.edu.

[†] Part of the special issue "Robert E. Wyatt Festschrift".

10.1021/jp072419i CCC: $37.00

namic equations of motion—the constraining factors on the quality of a QTM calculation are numerical in nature. By treating these numerical errors carefully one will obtain a solution that will be very close to the solution obtained by traditional methods (grid, pseudo-spectral, basis function expansions, etc.). By contrast, DPM consists of approximate equations of motion, and it will be seen that increasing the order of the real-valued DPM does not necessarily lead to the desired convergence properties. The DPM was extended to phase-space Wigner trajectories evolving under various master equations (Liouville, Wigner−Moyal, or Caldeira−Leggett)[30,31] and dissipative systems.[32,33] The real-valued DPM (RVDPM(n)) produces approximate quantum trajectories, but these trajectories are not correlated and can be propagated individually. Low-order DPM was shown to very accurately predict transmission probabilities in barrier scattering calculations in certain cases (when the width of the scattering potential barrier is greater than the width of the initial wave packet). However, very high orders must be used to obtain accurate results around nodes, and this presents numerical problems. By combining the initial value representation with the DPM, Bittner[34] was able to make observations concerning the utility of DPM with regards to certain types of problems. The DPM has been extended to high-dimensionality (10 degrees of freedom) barrier scattering problems.[35]

Recently, there has been interest in developing solutions to the complex-extended Hamilton−Jacobi equation for quantum mechanical problems. For stationary states, John[36] introduced complex trajectories in his analysis of the Hamilton−Jacobi equation. Yang has presented quantum trajectory solutions for the hydrogen atom,[37] the electronic spin motion,[38] the harmonic oscillator,[39] and tunneling dynamics.[40] Yang's solutions, however, require an analytic form of the wave packet at each step and thus are only applicable to situations in which the exact quantum mechanical solution is known a priori. Recently, Chou and Wyatt have presented a method for solving the complex Hamilton−Jacobi equation utilizing the Mobius propagation scheme. Excellent results were obtained for one-dimensional bound states[41] and scattering problems.[42,43] Boiron and Lombardi[44] ran complex semiclassical complex trajectories in 1998 that were successfully tested for some analytic as well as numerical cases. Recently, Goldfarb, Degani, and Tannor used the DPM to solve equations of motion for trajectories that had been extended to the complex plane.[45] This complex-extended DPM, denoted as CVDPM(n), was shown to very accurately reproduce barrier transmission probabilities at low orders, even for the deep barrier tunneling case. Perhaps the most interesting result of this study is that a very good approximation to the deep barrier tunneling probability is obtained with classical complex trajectories!

In this study, both RVDPM(n) and CVDPM(n) will be applied to model barrier scattering problems employing either an Eckart or a Gaussian barrier and an initial Gaussian wave packet. The initial wave packets in these calculations will have either zero initial energy, denoting a deep barrier tunneling problem (DT), or an initial energy equal to the barrier height, which is termed high-energy (HE). Various properties of CVDPM(n) trajectories will then be examined. Of concern here is the method by which the appropriate initial conditions are chosen, the complex extension and influence of the potentials, and the behavior of CVDPM(n) trajectories in the complex plane for several orders of DPM.

In the next section, relevant equations of motion for both RVDPM(n) and CVDPM(n) trajectories will be presented and discussed. Then, in section 3, implementation issues, computational methods, and the model problem involving Eckart and Gaussian potentials will be discussed. Section 4 presents relevant results for both DT and HE scattering from Eckart and Gaussian barriers as well as analysis of some complex quantum trajectories. Finally, concluding remarks will be given in section 5.

2. Theory

2.1. Real-Valued Quantum Trajectories. In this section, the real-valued DPM equations of motion will be derived and discussed in both the Eulerian and the Lagrangian frames. A discussion of the conservation of weights on real-valued quantum trajectories will follow. Equations for CVDPM(n) will be derived and discussed in subsection 2.2, in both the Eulerian and the Lagrangian frames. Finally, this section will close with an analysis of CVDPM(2) trajectories.

Equations of motion for real-valued quantum trajectories are obtained by first performing a polar decomposition of the wave function, via the ansatz

$$\Psi(x,t) = \exp\left(C(x,t) + \frac{i}{\hbar} S(x,t)\right) \tag{1}$$

In eq 1, $S(x,t)$ is the real-valued action function, and $C(x,t)$ is a real-valued function that is related to wave function density via $\rho(x,t) = |\psi(x,t)|^2 = \exp(2C(x,t))$. Substituting eq 1 into the TDSE and separating the resulting equation into real and imaginary parts yield two coupled equations. The first is the quantum Hamilton−Jacobi equation

$$\frac{\partial S(x,t)}{\partial t} + \frac{1}{2m}{S_1}^2 + Q_B + V = 0 \tag{2}$$

where Q_B represents the nonlocal Bohm quantum potential

$$Q_B = -\frac{\hbar^2}{2m}[C_2 + {C_1}^2] \tag{3}$$

The second equation is the continuity equation

$$\frac{\partial C(x,t)}{\partial t} + \frac{1}{2m}[S_2 + 2C_1S_1] = 0 \tag{4}$$

In all equations, subscript notation is used for spatial partial derivatives

$$\frac{\partial^n F(q,t)}{\partial q^n} = F_n \tag{5}$$

where $q = x$ for real-valued trajectories and $q = z$ for complex-valued trajectories. These equations are cast in the Eulerian form (the grid points are stationary).

To obtain equations of motion for trajectories, it will be necessary to transform the Eulerian equations into the Lagrangian frame via the transform

$$\frac{d}{dt} = \frac{\partial}{\partial t} + v\frac{d}{dq} \tag{6}$$

where v is the flow velocity. Taking the de Broglie guidance condition, $p = S_1$, the flow velocity becomes

$$v = \frac{S_1}{m} \tag{7}$$

Substituting eqs 2 and 4 into eq 6 and using eq 7 yield Lagrangian equations for the evolution of the action

$$\frac{\mathrm{d}S(x,t)}{\mathrm{d}t} = \frac{1}{2m} {S_1}^2 - V + \frac{\hbar^2}{2m}[C_2 + {C_1}^2] \tag{8}$$

and the *C*-amplitude

$$\frac{\mathrm{d}C(x,t)}{\mathrm{d}t} = -\frac{1}{2m} S_2 \tag{9}$$

One way to propagate the trajectories described in eqs 8 and 9 is to employ the QTM.[2,13] In essence, this involves the propagation of a correlated ensemble of trajectories. At each time step, fitting techniques (such as least squares) can be employed to compute the spatial derivatives of the *S* and *C* functions to update the trajectory position and density. In this way, quantum nonlocality is explicitly introduced into the trajectory dynamics. However, as the trajectories evolve, any semblance of an ordered grid quickly disappears. While successful in a variety of problems, the QTM is usually computationally intensive.

Alternatively, the DPM can be used to derive an exact set of equations of motion for the spatial derivatives of the *C* and *S* functions. The spatial derivatives of *S* and *C* will be propagated along individual trajectories, and the need for fitting is removed. The DPM equations are obtained by spatially differentiating both sides of each Eulerian equation, eqs 2 and 4:

$$\frac{\partial S_1}{\partial t} = -\frac{1}{m} S_1 S_2 + \frac{\hbar^2}{2m}[C_3 + 2C_1C_2] - V_1 \tag{10}$$

and

$$\frac{\partial C_1}{\partial t} = -\frac{1}{2m}[S_3 + 2C_1S_2 + 2C_2S_1] \tag{11}$$

These equations transform to the Lagrangian frame as

$$\frac{\mathrm{d}S_1}{\mathrm{d}t} = \frac{\hbar^2}{2m}[C_3 + 2C_1C_2] - V_1 \tag{12}$$

and

$$\frac{\mathrm{d}C_1}{\mathrm{d}t} = -\frac{1}{2m}[S_3 + 2C_1S_2] \tag{13}$$

The first term on the right-hand side of eq 12 is the Bohm quantum force, $-\partial Q_B/\partial x$. Note that eqs 12 and 13 exhibit both down-coupling to lower-order derivatives and up-coupling to higher-order derivatives, making these equations and ones for the higher-order derivatives an infinite but exact hierarchy. Eulerian equations for RVDPM(2) can be derived by taking the spatial derivative of eqs 10 and 11

$$\frac{\partial S_2}{\partial t} = -\frac{1}{m}(S_1S_3 + {S_2}^2) + \frac{\hbar^2}{2m}[C_4 + 2{C_2}^2 + 2C_1C_3] - V_2 \tag{14}$$

and

$$\frac{\partial C_2}{\partial t} = -\frac{1}{2m}[S_4 + 2C_1S_3 + 4C_2S_2 + 2S_1C_3] \tag{15}$$

These equations transform to the Lagrangian frame as

$$\frac{\mathrm{d}S_2}{\mathrm{d}t} = -\frac{1}{m}{S_2}^2 + \frac{\hbar^2}{2m}[C_4 + 2{C_2}^2 + 2C_1C_3] - V_2 \tag{16}$$

and

$$\frac{\mathrm{d}C_2}{\mathrm{d}t} = -\frac{1}{2m}[S_4 + 2C_1S_3 + 4C_2S_2] \tag{17}$$

Notice the up-coupling to higher-order derivatives in eqs 16 and 17.

Equations 12, 13, 16, and 17 will constitute a closed set of equations if spatial derivatives of the *C*-amplitude and *S* of orders greater than 3 vanish. Following this procedure, Lagrangian equations for any order of real-valued DPM can be obtained through the following infinite system of equations

$$\frac{\mathrm{d}C_n}{\mathrm{d}t} = -\frac{1}{2m}[S_{2+n} + 2(C_1S_1)_n] + \frac{1}{m}S_1C_{1+n} \tag{18}$$

and

$$\frac{\mathrm{d}S_n}{\mathrm{d}t} = -\frac{1}{2m}({S_1}^2)_n + \frac{\hbar^2}{2m}[C_{2+n} + ({C_1}^2)_n] - V_n + \frac{1}{m}S_1S_{1+n} \tag{19}$$

To make progress with the infinite hierarchy of equations, assume that the *C* and *S* functions are smooth enough to be approximated in the vicinity of a trajectory by polynomials

$$C(\xi,t) = \sum_{k=0}^{K} \frac{1}{k!} c_k(t)\xi^k \tag{20}$$

and

$$S(\xi,t) = \sum_{k=0}^{L} \frac{1}{k!} s_k(t)\xi^k \tag{21}$$

where ξ denotes the displacement from a trajectory at time *t*. Assuming quadratic expansions ($K = L = 2$) for both *C* and *S*, substituting into eqs 2, 4, 10, 11, 14, and 15, and letting $\xi \rightarrow 0$ give six coupled equations that are exactly the same as eqs 2, 4, 10, 11, 14, and 15, only these equations lack spatial derivatives of *C* and *S* greater than order 2. This shows that truncation of the derivative hierarchy is equivalent to assuming some level of polynomial smoothness for the *C* and *S* fields. Lagrangian equations for any RVDPM(*n*) can be obtained by working out the terms in eqs 18 and 19 and setting to zero all spatial derivatives of *S* and the *C*-amplitude with orders greater than *n*.

From the preceding arguments, it is seen that the DPM is a generalization of earlier studies conducted by Heller[46] on the use of frozen or thawed Gaussians in time-dependent semiclassical scattering processes, known as Gaussian wave packet dynamics (GWPD). The difference, however, is that the DPM can approximate the *C* and *S* fields along each trajectory to quadratic and higher orders whereas Heller's studies employed equations of motion for parameters in a Gaussian that approximated the global wave packet. Several methods that employ multiple Gaussians propagating along classical trajectories will also be mentioned. Shalashilin and Child have developed a method that employs multiple nonorthogonal traveling frozen Gaussians that are sampled by a Monte Carlo procedure.[47−49] This method has been applied to tunneling problems.[48] In addition, Martinez et al.[50−52] have developed the multiple spawning method wherein additional frozen Gaussians following classical trajectories are used to augment the basis set where they are needed to account for tunneling and nonadiabatic

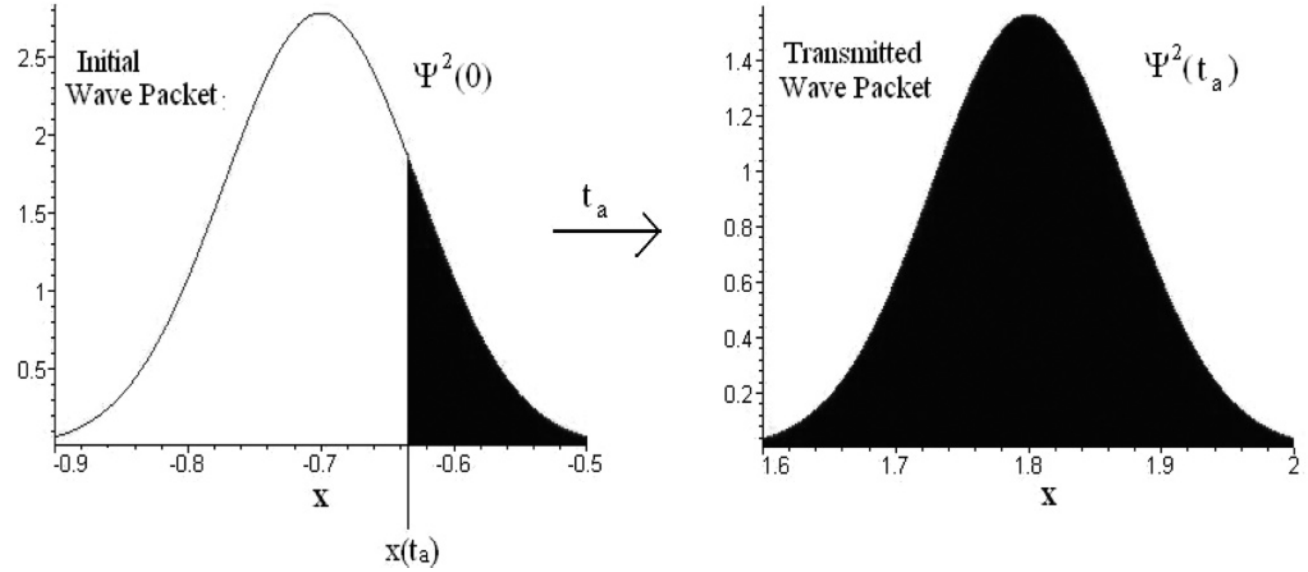

Figure 1. Integration of the initial Gaussian wave packet density from $x(t_a)$ forward yielding an area that is equal to the transmitted probability density at time t_a. The shaded region of $\Psi^2(0)$ represents the starting location of all trajectories that have transmitted the barrier at the arrival time t_a.

transitions. Much earlier studies by Metiu et al.[53] involved expansion of the wave packet in a swarm of thawed traveling Gaussians.

A few comments can be made about RVDPM(n) trajectories. First, note that these trajectories can be computed individually, and the need for functional fitting has been circumvented by propagating the approximate spatial derivatives of C and S along each trajectory. However, due to the up-coupling to higher-order spatial derivatives in the derivative propagation equations, the quantum potential will rarely be exactly specified along the trajectory. Higher orders of RVDPM(n) bring in improved approximations to the quantum potential and allow the trajectory to “sense” how the C and S fields are behaving in the vicinity of the trajectory. In this way, DPM can be thought of as introducing a regional nonlocality around each propagating trajectory. However, because the equations of RVDPM(n) are usually truncated at low order, the reach of this regional nonlocality is limited. High orders of RVDPM(n) are needed to allow distant features to affect the motion of the approximate quantum trajectory.

It is not necessary to propagate a large number of trajectories in a real-valued DPM calculation to obtain the transmission probability. The time-dependent transmission probability $P(t)$ of a wave packet through a barrier can be obtained via

$$P(t) = \sum_{i,\text{products}} w_i(x_i(t),t) \tag{22}$$

where w_i represents the trajectory weight[54] defined as

$$w_i(x_i(t),t) = \rho(x_i(t),t)\delta x_i \tag{23}$$

where δx_i represents a volume element. This weight is a conserved quantity,[54] as required by the continuity equation, eq 9. Recasting the weights in terms of the initial trajectory densities yields

$$w_i(x_i(t),t) = w_i(x_i(0),0) = \rho(x_i(0),0)\delta x_i \tag{24}$$

Substitution of eq 24 into eq 22 immediately shows that transmission probabilities can be computed only from the initial wave packet densities if one also knows which trajectories transmit the barrier. As shown in Figure 1, there is a definite bifurcation point for each time such that trajectories initially launched from the right of the bifurcation point will be transmitted while trajectories launched from the left will be reflected. Integrating the probability density obtained from the initial Gaussian wave packet from this bifurcation point forward will yield an area that is equivalent to the transmission probability at that time, in accordance with eq 22. Only a few transmitted trajectories need to be evaluated to locate the bifurcation point.

2.2. Complex-Valued Quantum Trajectories. Schrödinger recognized that the action S found in the Hamilton−Jacobi equation should be regarded as a complex quantity.[55] (He was motivated to make this change in an effort to consolidate both S and ρ into a single function.) Letting $z = x + \mathrm{i}y$ represent a point in the complex plane, we can express the complex-valued wave function in terms of a complex action $A(z,t)$ via the ansatz

$$\Psi(z,t) = \exp\left(\frac{\mathrm{i}}{\hbar}A(z,t)\right) \tag{25}$$

Inserting eq 25 into the TDSE yields a single complex equation

$$\frac{\partial A(z,t)}{\partial t} + \frac{1}{2m}{A_1}^2 + Q_\mathrm{C} + U = 0 \tag{26}$$

which is a complex version of the quantum Hamilton−Jacobi equation. (For an introduction, see section 4.2.3 in Tannor’s text.[56]) In this equation, Q_C represents a nonlocal complex quantum potential given by

$$Q_\mathrm{C} = -\frac{\mathrm{i}\hbar}{2m}A_2 \tag{27}$$

The de Broglie guidance condition, eq 7, is assumed valid, thus making the momentum complex. $U(z)$ is the continuation of the potential to the complex plane. The Lagrangian form of the complex quantum Hamilton−Jacobi equation can be obtained by substituting eq 26 into eq 6 and employing the guidance condition, thus giving

$$\frac{\mathrm{d}A(z,t)}{\mathrm{d}t} = \frac{1}{2m}{A_1}^2 - U + \frac{\mathrm{i}\hbar}{2m}A_2 \tag{28}$$

In effect, the Lagrangian transformation allows grid points to travel along complex quantum trajectories. The time-dependent wave function evaluated along the trajectory is given by

$$\Psi(z,t) = \exp\left\{\frac{\mathrm{i}}{\hbar}\left[A(z_\mathrm{o},0) + \int_0^t \frac{\mathrm{d}A(z,\tau)}{\mathrm{d}\tau}\,\mathrm{d}\tau\right]\right\} \tag{29}$$

with dA/dt given by eq 28. The density along the trajectory can be obtained through the relation $\rho(z,t) = \exp(-2/\hbar\ \mathrm{Im}(A(z,t)))$.

The derivative propagation method will again be employed to approximately solve eq 26. Note that, as in the real-valued case, the evolution equation for A requires the first- and second-order spatial derivatives of A to evaluate the expression. Evolution equations for these functions can be obtained by taking the first and second spatial derivatives of eq 26

$$\frac{\partial A_1}{\partial t} = -\frac{1}{m}A_1A_2 + \frac{\mathrm{i}\hbar}{2m}A_3 - U_1 \tag{30}$$

and

$$\frac{\partial A_2}{\partial t} = -\frac{1}{m}(A_2^{\ 2} + A_1A_3) + \frac{\mathrm{i}\hbar}{2m}A_4 - U_2 \tag{31}$$

Subsituting eqs 30 and 31 into eq 6 and employing the guidance condition give equations of motion in the Lagrangian frame

$$\frac{\mathrm{d}A_1}{\mathrm{d}t} = \frac{\mathrm{i}\hbar}{2m}A_3 - U_1 \tag{32}$$

and

$$\frac{\mathrm{d}A_2}{\mathrm{d}t} = -\frac{1}{m}A_2^{\ 2} + \frac{\mathrm{i}\hbar}{2m}A_4 - U_2 \tag{33}$$

The first term on the right-hand side of eq 32 is the complex-valued and nonlocal quantum force, $-\partial Q_\mathrm{C}/\partial z$. This quantum force is not the same function that appears on the right-hand side of the Bohmian equation, eq 12. For example, the Bohmian quantum force is anti-Hook's law (linear in displacement from the center and expansive) for a Gaussian wave packet, but the force term given by $-\partial Q_\mathrm{C}/\partial z$ vanishes. (Classical trajectories provide the exact propagation for the packet in the latter formulation.) The form of the quantum force in eq 32 may be the prime reason that low-order DPM calculations give excellent results for some barrier transmission problems (as described later in this study).

Lagrangian equations of any order can be generated using the following equation

$$\frac{\mathrm{d}A_n}{\mathrm{d}t} = -\frac{1}{2m}[(A_1^{\ 2})_n - \mathrm{i}\hbar A_{2+n}] + \frac{1}{m}A_1A_{1+n} - U_n \tag{34}$$

It was precisely CVDPM(n) that Tannor and co-workers[45] employed in their complex-valued trajectory study. A discussion of the correspondence between RVDPM(n) and CVDPM(n) is provided in the Appendix.

A brief examination of eqs 28 and 32 is in order. The right-hand side of eq 32 represents the components of force acting upon each trajectory. The local (or classical) force is contained in the derivative of the potential, while all quantum forces are represented by the $\hbar$-dependent A_3 term. Focusing upon second-order DPM leads to trajectories with purely Newtonian (albeit complex) motion, as the A_3-dependent quantum force will be zero. The trajectory is guided through completely local information contained in the derivative of the complex-extended "classical" potential. Note, however, that eq 28 includes a nonlocal quantum energy term A_2. The CVDPM(2) equation for A_2

$$\frac{\mathrm{d}A_2}{\mathrm{d}t} = -\frac{1}{m}A_2^{\ 2} - U_2 \tag{35}$$

includes both local information (from the derivative of the complex potential) and nonlocal information (through the derivative of A this information is considered to be nonlocal as it depends on the state of the entire wave function). This serves to introduce nonlocality into eq 28 and consequently into eq 29, which accumulates the appropriate quantum phase for wave function synthesis at each time step. In effect, CVDPM-(2) trajectories are classical trajectories traveling in the complex plane—quantum information is only manifested thorough the quantum potential appearing in the action function.

Equation 33 shows that the trajectory will no longer exhibit classical motion for CVDPM(3), as an approximation to the quantum force influences the trajectory motion. This has an interesting effect on the interpretation of tunneling in the complex plane. CVDPM(2) trajectories are classical in the sense that only local information provided by the potential is used to propagate the trajectory. These trajectories are ones that make it over the top of the barrier—they do not "go through the barrier". However, each CVDPM(2) trajectory is carrying a density that ultimately will make it to the real axis at the arrival time and be "detected". The net effect of this density transport on the complex-classical trajectory is to make it appear as if the low-energy initial wave packet "tunnels" through the classically forbidden region and appears on the transmission side of the barrier.

Interestingly, the CVDPM(2) equations appeared in the literature before the recent publication by Tannor et al.[45] In generalizing earlier work with GWPD, Huber and Heller[57] extended the classical trajectories into the complex plane and in effect generated the equations of motion for CVDPM(2) trajectories. Subsequent collaboration with Littlejohn[58] provided deeper mathematical insight into these trajectories. Again, as in the case of RVDPM(n), our formulation has the advantage in that we approximate $A(z,t)$ in a quadratic or higher-order expansion along each propagating trajectory, as opposed to a global "thawed" Gaussian. de Aguiar and co-workers[59] expanded upon this work by Heller by deriving additional approximations to replace the complex trajectories with real trajectories. These studies are semiclassical; it is important to remember that the infinite heirarchy of DPM equations of motion is exactly quantum.

3. Model Scattering Problem and Computational Methods

In this section, the initial wave packet and the two potentials are described. The implementation of both RVDPM(n) and CVDPM(n) trajectories will also be discussed. Finally, for comparison with the trajectory results, a space-fixed grid method for solving the TDSE for these scattering problems will be mentioned. All calculations were run to the arrival time $t_\mathrm{a} = 1.5$. Unless otherwise stated, all quantities are in atomic units.

The initial conditions on individual trajectories were determined from a Gaussian wave packet of the form

$$\Psi(x) = \left(\frac{2\beta}{\pi}\right)^{1/4} \exp\left(-\beta(x - x_\mathrm{o})^2 + \frac{\mathrm{i}p_\mathrm{o}}{\hbar}(x - x_\mathrm{o})\right) \tag{36}$$

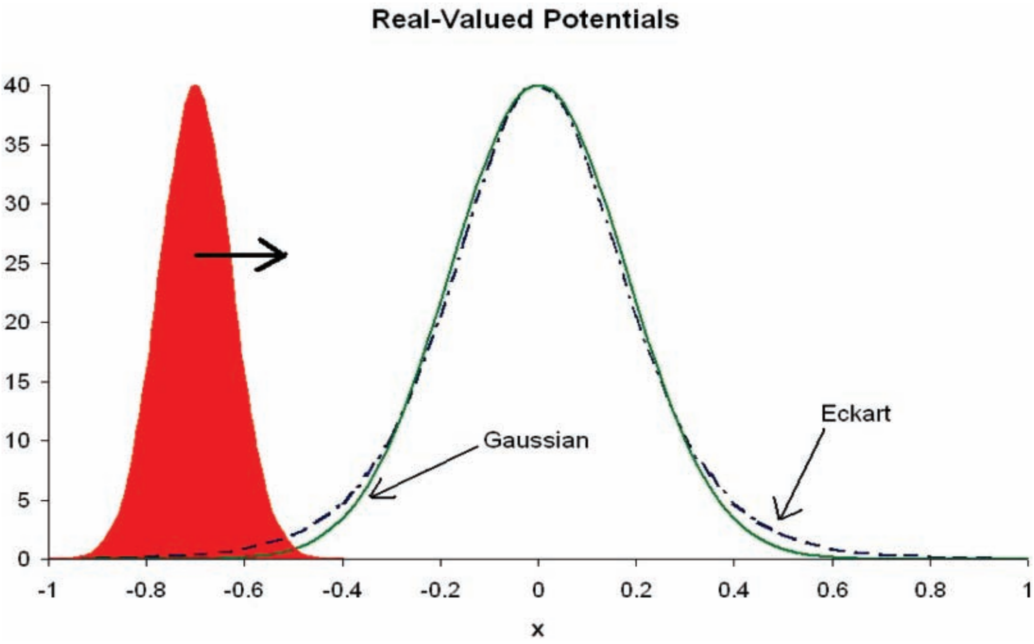

Figure 2. Real-valued Eckart (in blue) and Gaussian (in green) potentials used in this study. The magnitude of the initial Gaussian wave function (solid red) is also shown to compare the relative width of the wave packet to the barrier width. For the purposes of this figure, the peak value for $|\Psi(x)|$ was adjusted to be the same as the barrier height.

This function is normalized on the real axis. Following Tannor et al.,[45] we choose the width parameter $\beta = 30\pi$, the center of the wave packet $x_o = -0.7$, and the initial momentum either $p_o = 0$ (DT case) or 48.9 (HE case). Initial conditions for complex trajectories were obtained by analytically continuing eq 36 into the complex plane.

Obtaining the initial functional values required for the time integration of the RVDPM(n) trajectories is straightforward. Equating the right-hand sides of eqs 1 and 36 and separating into real and imaginary parts lead to functions that give the initial values of $C(x,t)$ and $S(x,t)$ in terms of the parameters in eq 36 for any given selected initial x value.

Obtaining initial functional values for CVDPM(n) is a more difficult task. Equating the right-hand sides of eqs 25 and 36 leads to a single equation that returns the initial value of $A(z,t)$ with regard to the parameters in eq 36 and the initial coordinate z. For CVDPM(n), one obtains the initial coordinates z by merely discretizing the complex extension of the initial wave packet. However, both the real and the imaginary parts of z are discretized to obtain the initial condition. Trajectories with the same initial real part but different imaginary parts in their complex positions will have drastically different behaviors. The trajectories of interest will be those that have position $y = 0$ at the specified arrival time and $x > 0$ for the transmitted subset. The imaginary component of the complex initial position has a direct effect on both the time and the position where these trajectories cross the real axis. The set of initial complex positions z that satisfy the above condition will comprise a curve in the complex plane called an isochrone. Any trajectory launched from an initial position on that isochrone will land somewhere on the real axis ($x > 0$, $y = 0$) at the specified arrival time. Properties of isochrones will be discussed further in section 4.2.

The potentials used for both the real and the complex trajectory calculations are either an Eckart barrier of the form

$$V(z) = \frac{V_o}{\cosh^2(\alpha z)} \tag{37}$$

where the barrier height is $V_o = 40$ and the barrier width parameter is $\alpha = 4.32$ or a slightly slimmer Gaussian barrier of the form

$$V(z) = V_o \exp(-\gamma z^2) \tag{38}$$

where again $V_o = 40$ and the width parameter is $\gamma = 15.35$. Both barriers are centered at $z = 0$. The two potentials evaluated on the real axis are shown in Figure 2, while the real and imaginary parts of the complex-extended Eckart potentials are shown in Figures 3a and 3b, and the real and imaginary parts of the complex-extended Gaussian potential in Figures 4a and 4b, respectively.

Figure 2 shows that we are dealing with a “thick” barrier scattering problem, in that the half-width of the initial Gaussian wave packet is slim compared to the width of the scattering Eckart and Gaussian potentials. Thick barrier quantum scattering problems typically display transmitted probability densities that are similar to those produced by the propagation of the corresponding Wigner wave packet in phase space with the classical Liouville equation. Alternatively, one can obtain classical transmitted probability densities in phase space by integrating the initial Wigner wave packet for $p \geq p_b$, where p_b represents the barrier momentum. An example of the similarity of phase-space classical and quantum barrier transmission probabilities is presented by Rowland and Wyatt.[60] Thin barrier scattering problems will have solutions that depend much more strongly upon the quantum potential and are not reproduced nearly as well with classical phase-space methods.

Given the Cauchy−Riemann condition[61] for the complex-valued function $f(x + iy)$, i $\partial f/\partial x = \partial f/\partial y$, we can determine whether or not the potentials given in eqs 37 and 38 are analytic. The Cauchy−Riemann condition is seen to hold for the Gaussian potential in eq 38 in the domain of the finite complex plane. Hence, this complex-extended potential would be termed holomorphic;[61] that is, the potential has no singularities and is differentiable at every point in the finite complex plane. Application of the Cauchy−Riemann condition to eq 37 shows that the complex-extended Eckart potential is meromorphic;[61]

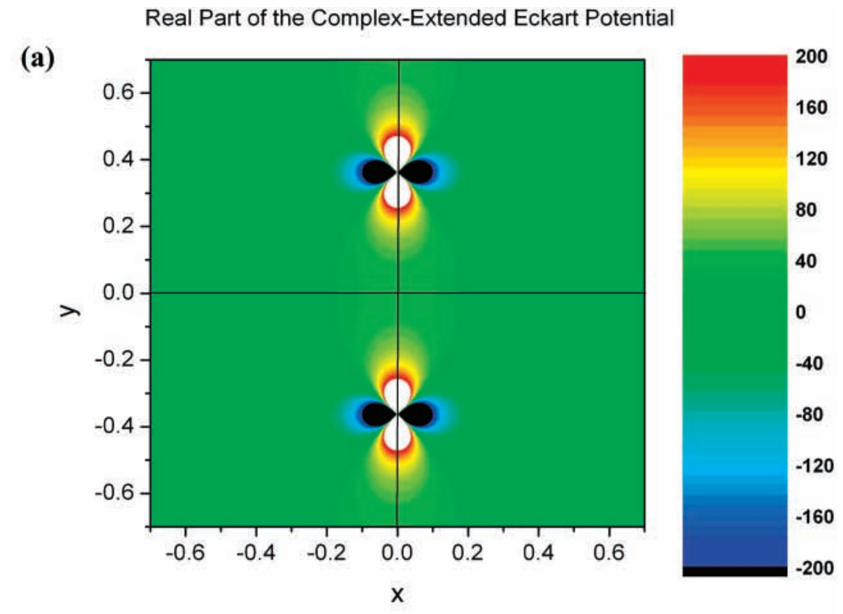

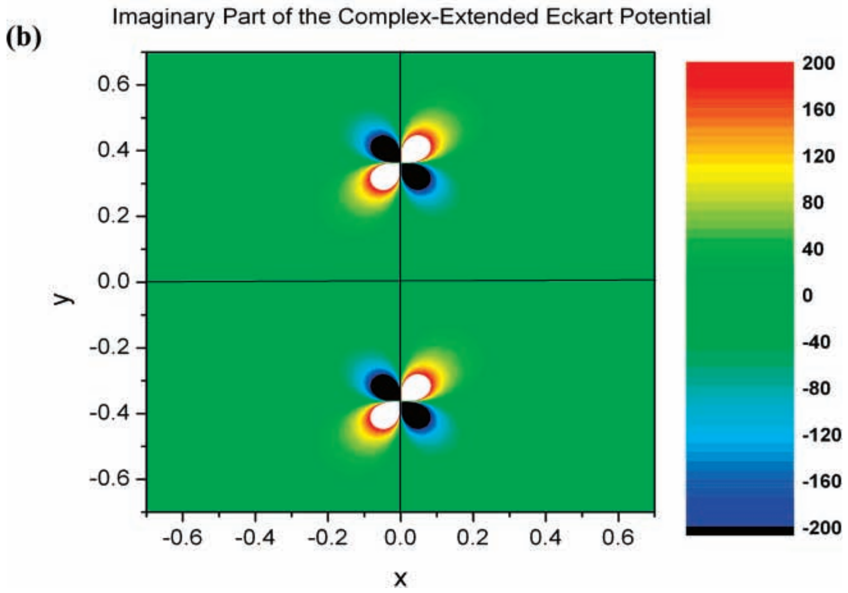

Figure 3. Complex-extended Eckart potential: (a) real part; (b) imaginary part.

that is, it is analytic in the finite complex plane at all but some isolated points. These isolated points (albeit countably many) are the poles of the complex-extended Eckart potential. These poles, at the centers of the cloverleafs along the imaginary axis in Figures 3a and 3b, are located at

$$z = \frac{m\pi}{2\alpha}\mathrm{i} \tag{39}$$

where $m = \pm 1, \pm 2, ...$ The two poles of principal interest are located at $z = \pm 0.3636\mathrm{i}$. Later, it will be seen that complex trajectories are forced to avoid the poles in the complex-extended Eckart potential. Very interesting behavior is also obtained for complex trajectories evolving on the complex-extended Gaussian potential.

An examination into the nature of the poles in the complex-extended Eckart potential is in order. Specifically, we would like to examine the behavior of the potential in the vicinity of the pole as well as explain the four-lobed structures and associated signs that appear in Figures 3a and 3b. One way to approach this problem is to expand the complex-extended Eckart potential about a pole using a Laurent series.[62] A Laurent series can be thought of as an extension of the Taylor series to complex functions that are meromorphic. Unlike the Taylor series, which only employ positive powers in the power series expansion, a Laurent series may employ negative powers in the expansion

$$f(z) = \sum_{n=-\infty}^{\infty} a_n (z - z_o)^n \tag{40}$$

where the expansion coefficients a_n are given by Cauchy's integral formula. Performing a Laurent expansion on eq 37 about the node located at $z_o = -\mathrm{i}\pi/2\alpha$ gives

$$V(z_o) = -\frac{V_o}{\alpha^2}\frac{1}{(z - z_o)^2} + \frac{1}{3}V_o - \frac{1}{15}V_o\alpha^2(z - z_o)^2 + \frac{2}{189}V_o\alpha^4(z - z_o)^4 + O((z - z_o)^6) \tag{41}$$

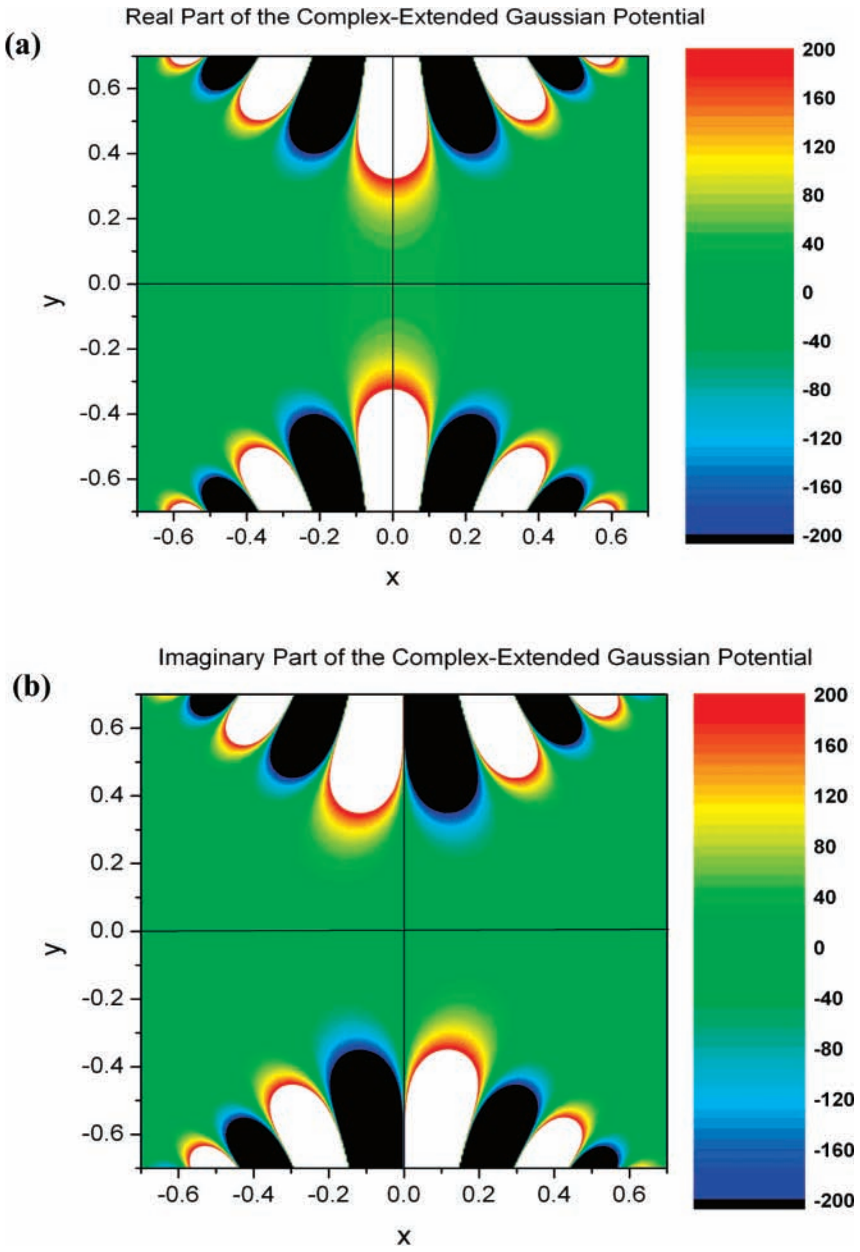

Figure 4. Complex-extended Gaussian potential: (a) real part; (b) imaginary part.

where the first term in eq 41 is known as the principle part of the function. Notice that a holomorphic function will have no principle part.

Determining the order of the pole is a simple matter with eq 41; all one must do is look to the principle part of the Laurent expansion. In this example, we see that the poles of the complex-extended Eckart barrier are of second order (this means that the residue about the poles will be zero); these poles are neither simple poles (poles of order one, also known as removable singularities) nor are they essential singularities (which would have an infinite number of terms in its principle part). The principle part of the Laurent series describes the behavior of the function in the vicinity of the pole. As one approaches z_o only the principle part of the expansion contributes, up to an additive constant. Simply put, $(z - z_o) = Re^{i\theta}$ (the expression of a complex number in polar form). Combining the above expression with the principle part of eq 41 gives

$$V(z_o) \rightarrow -\frac{V_o}{\alpha^2}\frac{1}{R^2}\exp(-2i\theta) \tag{42}$$

Plotting the real and imaginary parts of this function will reproduce the four-lobed “quadrapole” structures as well as the signs on those lobes in agreement with Figures 3a and 3b.

A similar analysis can be carried out for the Gaussian potential. Making the subsitution $z = 1/t$ in equation eq 38 and performing a Taylor series expansion yields

$$V\left(\frac{1}{t}\right) \rightarrow 1 - \frac{\gamma}{t^2} + \frac{\gamma^2}{2t^4} + O\left(\frac{1}{t^6}\right) \tag{43}$$

Bearing in mind that as $z \rightarrow \pm\infty$, $t \rightarrow 0$, so the function is not defined at $\pm\infty$. These will be singularities in the Gaussian potential. The expansion in eq 43 tells us that these singularities will be isolated essential singularities[61] as the principle part of its expansion has an infinite number of terms.

Holomorphic and meromorphic (excluding poles) functions have very interesting properties that cast a different flavor on CVDPM(n) trajectories. If a function $f(z)$ is holomorphic both inside and on a simple closed contour C in the complex plane, then the generalized Cauchy integral formula guarantees the existence of the derivatives (including partials) of $f(z)$ of all orders.[62] These derivatives will be continuous both on and inside the contour C. No similar statement can be made for real functions.

The Cauchy integral formula also states that the value of $f(z)$ at any point z inside the closed contour C will be determined by the values of the function along C. This is very interesting in the context of complex DPM trajectories. Complex DPM trajectories can "sense" the behavior of their neighbors through a regional nonlocality. The potentials and the evolving wave packet remain holomorphic as long as they stay in the finite complex plane (both Eckart and Gaussian potentials) and avoid poles (Eckart potential only). This means that the value of the wave packet at any point z in the complex plane is determined solely by the values of the wave packet on a closed contour. In other words, the value of the function $f(z)$ depends on information at other points (i.e., nonlocality). This may explain why low orders of CVDPM(n) can yield very accurate barrier transmission probabilites.

Equations of motion for both RVDPM(n) and CVDPM(n) trajectories were implemented by integrating the system of differential equations in time with the second-order implicit trapezoidal method.[63] This method is both symmetric and self-adjoint, which ensures time reversibility. DPM equations for barrier scattering problems can become stiff in regions where the derivatives of the action may become large (i.e., near a pole). Stating that a system of differential equations is stiff generally means that the dynamical processes being modeled are evolving under multiple time scales.[64] Another way to think of stiffness is that the largest allowable step size taken is determined by the system's stability rather than the accuracy. The implicit trapezoidal method was chosen to integrate this system of differential equations because it is a relatively easy method to implement and is known to handle stiff systems of differential equations well. Solving this system of nonlinear equations requires the use of functional iteration or Newton's method. In this study, functional iteration was used with the initial guess given by the first-order explicit Euler method. Three functional iterations were sufficient at each time step. In both RVDPM(n) and CVDPM(n), the integration time step was $\Delta t = 1 \times 10^{-4}$.

To solve the TDSE on a grid,[64,56] the method of lines[63] was employed with fourth order centered finite differencing to obtain a system of differential equations that was integrated using the second-order leapfrog method.[63] The leapfrog method is not symplectic, however. This was not a problem in this study, as the normalization on the entire grid remained accurate to 10^{-5} for the length of the calculation. The grid calculation used to solve the TDSE was performed with $\Delta t = 1 \times 10^{-4}$ and $\Delta x = 5 \times 10^{-3}$.

4. Computational Results

4.1. Transmission Probabilities. In this section, transmission probabilities will be presented for RVDPM(n) and CVDPM(n) trajectories for both the Eckart and the Gaussian barrier scattering problems. This will be followed by results and discussion for classical complex trajectories (CVDPM(2)). Determining how initial conditions are implemented into CVDPM(n) is discussed in subsection 4.2. Finally, some interesting properties of complex quantum trajectories will be explored.

TABLE 1: Transmission Probabilities for RVDPM and CVDPM Barrier Scattering Problems

order of DPM	probability
DT Eckart Real Valued	
5	2.79×10^{-7}
6	3.77×10^{-7}
7	3.11×10^{-7}
8	3.34×10^{-7}
9	3.19×10^{-7}
fixed grid (exact)	2.90×10^{-7}
HE Gaussian Real Valued	
2	0.504740
3	0.503410
4	0.500900
5	0.487960
6	0.419330
fixed grid (exact)	0.502366
DT Eckart Complex Valued	
2	2.77×10^{-7}
3	2.90×10^{-7}
4	2.90×10^{-7}
fixed grid (exact)	2.90×10^{-7}
HE Gaussian Complex Valued	
2	0.503070
3	0.507320
4	0.501710
fixed grid (exact)	0.502366

Table 1 lists transmission probabilities for real-valued DPM trajectories for the DT Eckart and HE Gaussian scattering problems. There are some points of note here. First, it appears that the appropriate order of real-valued DPM can give transmitted densities that are close to the exact grid solution. In the case of the HE Gaussian scattering problem, orders 2, 3, and 4 give results that are in good agreement with the exact grid results, whether the final probability is computed by actually interpolating the transmitted wave packet density and integrating or by locating the bifurcation point and integrating the initial probability density. However, it is interesting to see that the probabilities for real-valued DPM do not appear to converge smoothly as the order is increased. Similar trends are noted for the HE Eckart scattering problem. Figure 5a shows HE Eckart transmitted probability densities for orders 2 and 3 for real-valued DPM. RVDPM(2) and RVDPM(3) reproduce the exact grid solution. As the order of the DPM is increased to orders 4 and 5, the integrated probabilities correspond quite well with the numerical probabilities provided by the fixed-grid solution.

The DT Gaussian scattering problem shows different characteristics. First, accurate solutions require higher orders of DPM than the corresponding HE case. Figure 5b shows DT Gaussian transmitted probability densities for orders 8−12 of RVDPM. There appears to be an oscillation about an average value, with even orders of RVDPM slightly overestimating the probability and odd orders being just about right.

Figures 6a and 6b show corresponding CVDPM(n) transmitted probability densities for orders 2, 3, and 4 for the same scattering problems as presented in Figures 5a and 5b. Initial positions for these trajectories are specifically chosen so that they transmit the barrier ($x > 0$) and are detectable ($y = 0$) at the arrival time $t_a = 1.5$. Figure 6a shows the transmitted densities for the HE Eckart barrier scattering problem for orders 2−4. This figure shows that orders 2, 3, and 4 perfectly capture the grid solution, with no detectable decay in the quality of solution. Figure 6b shows the transmitted densities for the DT Gaussian barrier scattering problem for orders 2−4. Note that orders 3 and 4 capture the solution exactly. Although CVDPM(2) does not quite capture the exact solution, we need to recall that CVDPM(2) trajectories are in fact complex-valued classical trajectories transporting an approximate quantum action function (through the inclusion of the nonlocal term in eq 28). In essence, these trajectories appear to tunnel through the barrier, when in

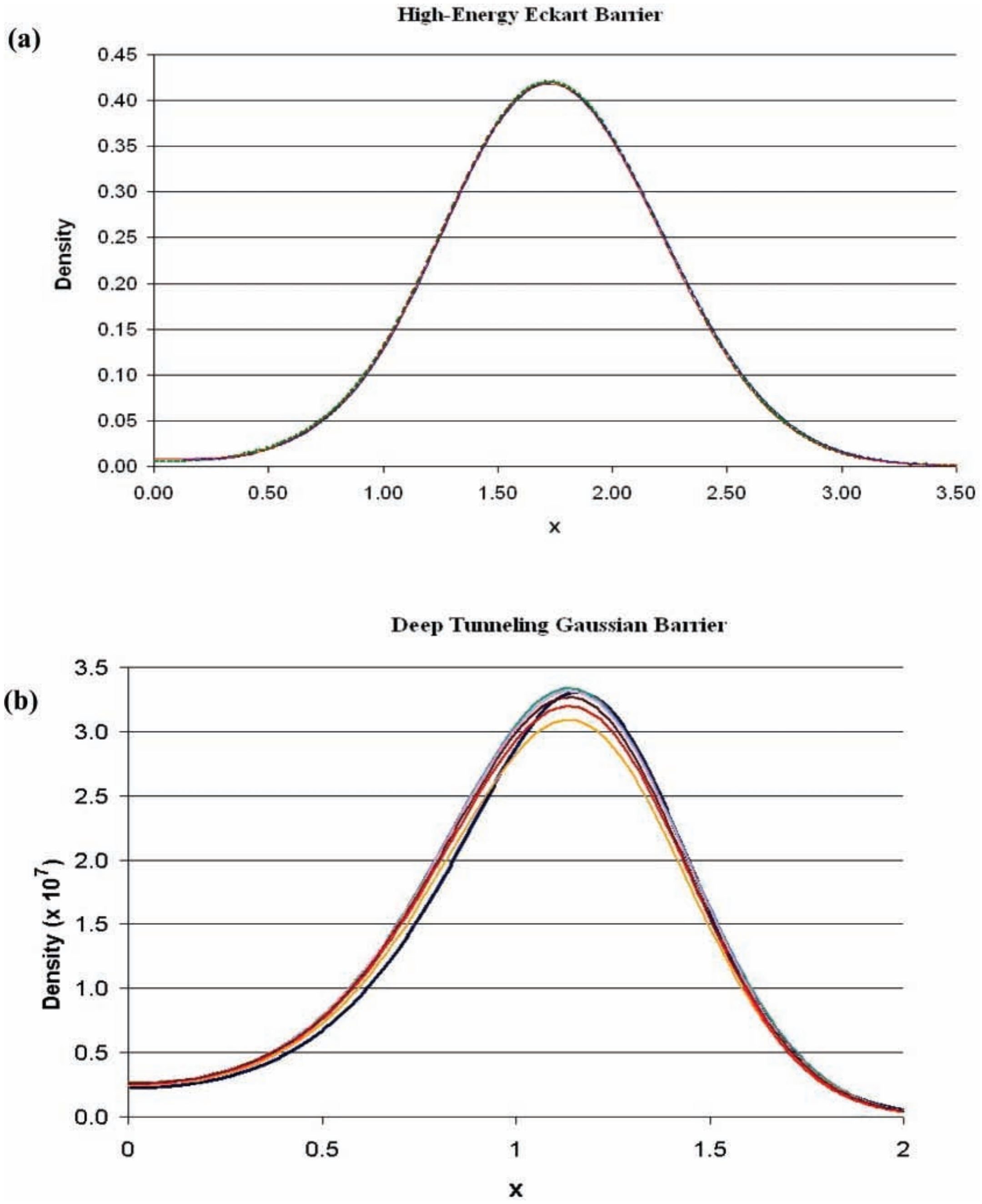

Figure 5. RVDPM(n) transmitted probability densities at $t_a = 1.5$: (a) HE Eckart barrier densities for $n = 2$ (blue), 3 (red), and grid (dark green) solutions; (b) DT Gaussian densities for $n = 8$ (orange), 9 (green), 10 (red), 11 (purple), 12 (brown), and grid (dark blue).

reality they are following classically proscribed paths through the complex plane while transporting approximate quantum density. Increasing CVDPM to order 3 adds an approximation to the quantum force to the classical force when computing the trajectory. Note that the CVDPM(n) solutions remain in agreement with the grid solution through order 4. Similar accuracies and trends are noted in the DT Eckart problem and in the HE Gaussian problem. CVDPM(n) was run through order 6 for these four problems with no decay in the solution quality.

4.2. Isochrones. Figure 7 shows nine CVDPM(2) trajectories (blue curves) for the arrival time $t_a = 1.5$. Also shown are contour lines for the absolute value of the complex-extended Eckart potential. These trajectories are launched from a curve in the complex plane—the isochrone. Some of the characteristics of isochrones will now be considered. Figure 8a shows the isochrones for the DT Eckart scattering problem for CVDPM(n) orders 2, 3, and 4. Notice that the isochrones traverse only a small portion of the complex plane. The order 2 isochrone converges on the x-coordinate of the center of the initial wave packet ($x_c = -0.7$) but does not extend to values of x that are less than this. This point represents the initial coordinate of the last detectable, transmitted complex trajectory. Increasing the order to CVDPM(3) changes the isochrone in two ways. First, each point is shifted down in the imaginary direction. Since these trajectories will be traveling farther than corresponding CVDPM(2) trajectories and they still need to reach the real axis at $t_a = 1.5$, they need to traverse this distance faster. To understand this further, one must understand how the real and imaginary components of the complex-extended potential are manifesting themselves upon the trajectory, which will be examined later in subsection 4.4. Second, unlike CVDPM(2) trajectories, it is seen that higher-order isochrones extend to the

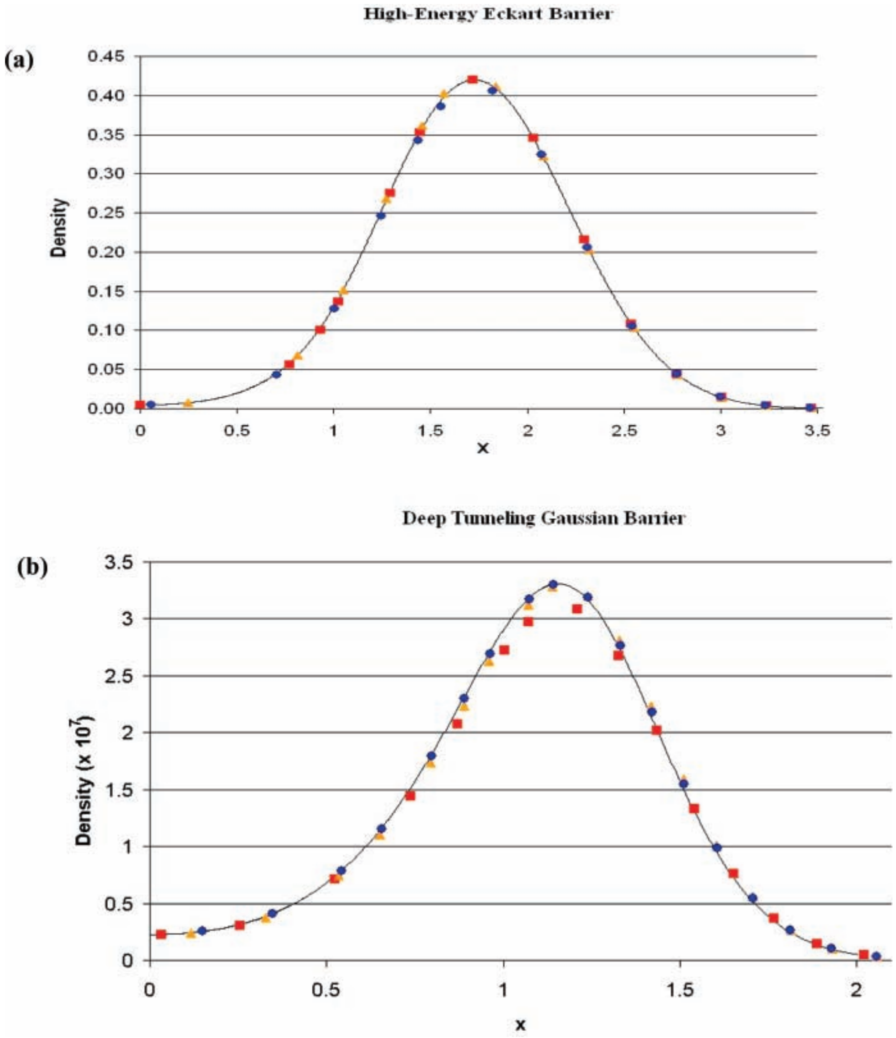

Figure 6. CVDPM(n) transmitted probability densities at $t_a = 1.5$ for $n = 2$ (red squares), 3 (orange triangles), 4 (blue circles), and grid (black line): (a) HE Eckart barrier solutions; (b) DT Gaussian solutions. Notice that CVDPM(2) (classical) trajectories capture the essence of the solution.

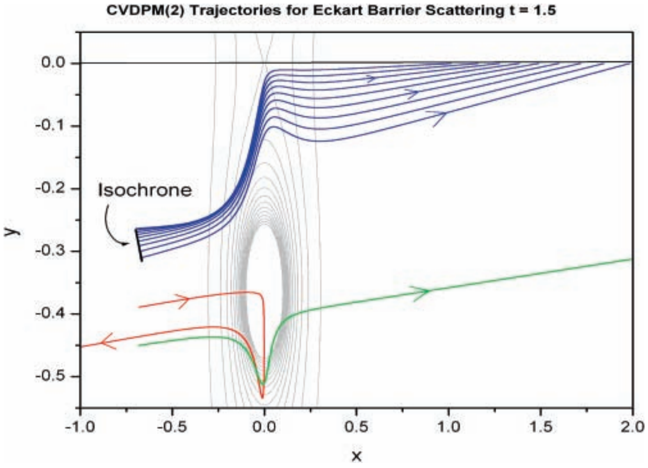

Figure 7. Classical complex trajectories for the deep tunneling Eckart barrier scattering problem, with contours of the absolute value of the complex-extended Eckart potential. Note how the detected transmitted trajectories with the arrival time $t_a = 1.5$ (shown in blue) bend away from the pole on the imaginary axis (at $z = -0.35i$) in a manner reminiscent of Rutherford foil scattering. The green trajectory is also transmitted, but it is not detected until a time $t > 1.5$. The red trajectory is back-scattered from the potential and is undetected at $t_a = 1.5$.

left of the center of the initial wave packet. These trajectories have different properties than those launched with $x > -0.7$. These trajectories will be analyzed further in subsection 4.4.

Figure 8b shows similar behavior to that found in Figure 8a, but for HE scattering from the Eckart barrier. It is interesting to note that all three isochrones converge on the real axis, but at different locations. CVDPM(2) trajectories exhibit the same convergence at the center of the wave packet as seen for the DT Eckart scattering problem in Figure 8a. CVDPM(3) and CVDPM(4) lead to very nearly the same isochrone. Isochrones for initial energies between DT and HE barrier scattering will lie between these extremes. Isochrones for both the DT and the HE Gaussian barrier problems show similar placements and trends as the Eckart cases. It is interesting to note that the isochrones appear to converge for orders 3 or 4 for all cases.

Obtaining the locations of the isochrones proves to be the most difficult part of implementing CVDPM(n). Initial coordinates were obtained by taking a slice for a constant value for y and selecting x to be between 0 and x_o. This will yield initial values for $A(z,t)$ and its spatial derivatives, which allows one to integrate the trajectory equations. The final location of this trajectory in the complex plane was noted at the preset arrival time t_a, and the initial x-coordinate was varied to allow the trajectory to cross the real axis at the arrival time. This is similar to finding the bifurcation point in the real-valued DPM problem; however, this calculation must be repeated many times at different values of y to define the isochrone. It is also possible to fit a high-order polynomial to a few data points (once they have been obtained) to help predict the location of the

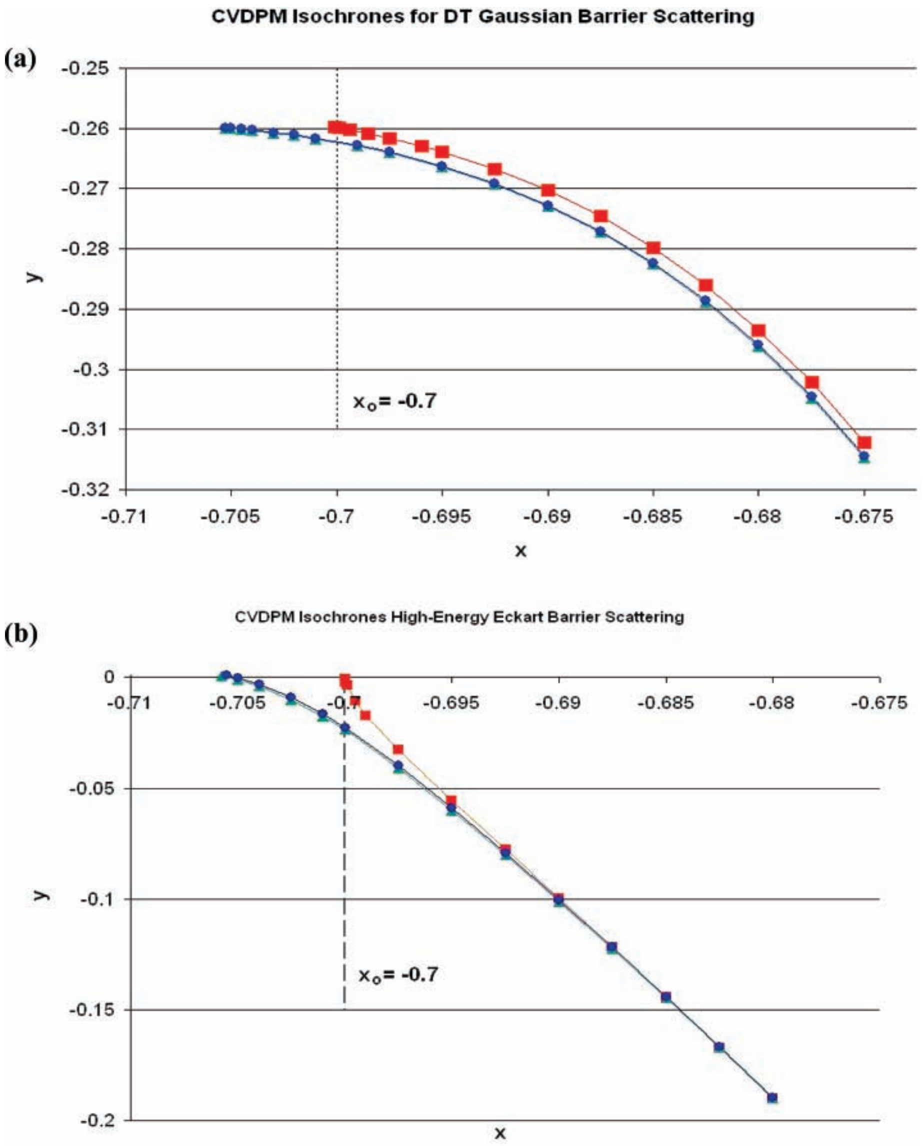

Figure 8. CVDPM(n) isochrones for the arrival time $t_a = 1.5$: $n = 2$ (red squares), 3 (dark green triangles), and 4 (blue circles): (a) DT Eckart scattering problem; (b) HE Eckart scattering problem. Notice that in both cases the CVDPM(2) isochrones terminate at the x-coordinate of the initial wave packet, x_o, while CVDPM(3) and CVDPM(4) isochrones continue smoothly past this point.

isochrone.[65] In this way, the search procedure could be automated, but that was not done in this study.

4.3. Classical Complex Trajectories. In this subsection, some properties of CVDPM(2) trajectories will be explored. Figure 7 reveals that different initial coordinates may lead to drastically different effects during the evolution of the complex trajectories. The potential energy contours show that these trajectories are interacting with the pole centered around $z = -0.35i$. The reactive trajectories (in blue) with $t_a = 1.5$ can be seen deflecting around the top of this pole, while one transmitted trajectory (green curve) with $t_a > 1.5$ skirts around the lower edge of this pole. A nontransmitted trajectory (red curve) is also shown. Note how this trajectory appears to enter the barrier region but is repelled by the pole; this trajectory is unlucky enough to have initial conditions that lead it directly toward this pole.

The behavior of these trajectories suggests that a force analysis of CVDPM(2) trajectories will be instructive. Figure 9a shows two CVDPM(2) trajectories, one transmitted and one back-scattered for the DT Eckart problem. The arrows represent the vectors of force, $-dV/dz$, for the complex-extended Eckart potential. These trajectories follow classical paths, and it is interesting to see how they are influenced by the complex-valued force. Notice that the trajectories follow the lines of force.

To make further progress, we will examine the initial velocities of the trajectories. This velocity as a function of the complex position is given by

$$v_{\text{initial}}(z) = -\frac{i\hbar}{m}\left(-2\beta(z - x_o) + \frac{ip_o}{\hbar}\right) = \left(\frac{p_o}{m} - \frac{2\hbar\beta}{m}y\right) + i\,\frac{2\hbar\beta}{m}(x - x_o) \quad (44)$$

For the DT case, $p_o = 0$. It is seen that the real part of the initial velocity when $y = 0$ is just as expected, p_o/m. Of interest are both the real and the imaginary parts of the initial velocity. This equation reveals that trajectories launched from below the real axis ($y < 0$) will have a positive x component. For trajectories initiating to the right of the center of the wave packet ($x > x_o$), the initial velocity will contain a component in the positive y direction. Figure 10a shows a plot of eq 44 for the DT Guassian scattering problem while Figure 10b shows a plot for the HE Eckart scattering problem. These figures also show CVDPM(2) and CVDPM(3) isochrones for these scattering

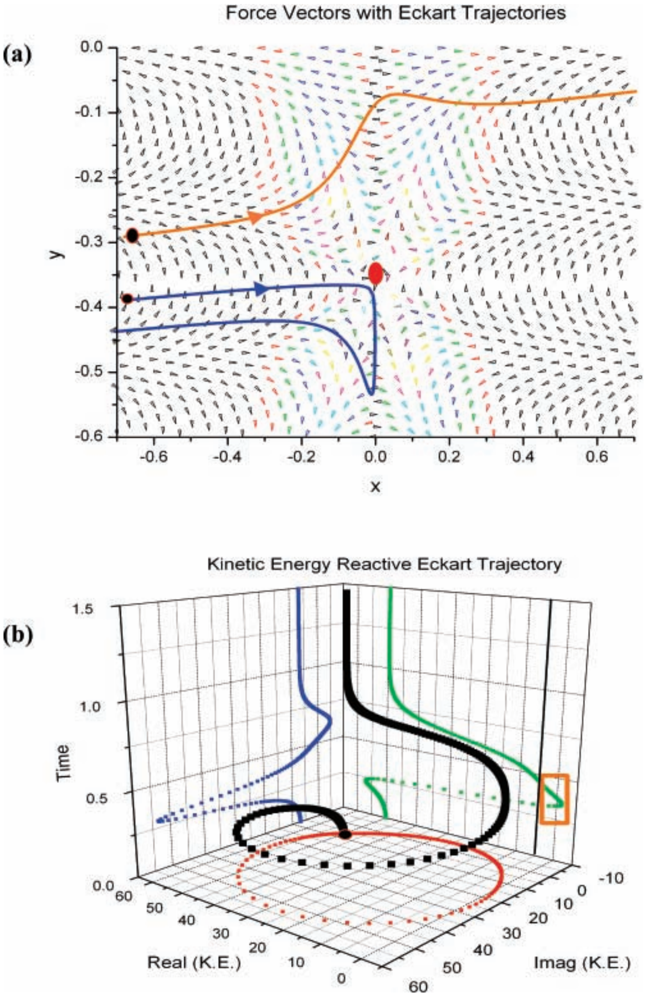

Figure 9. Classical complex trajectories for the Eckart deep tunneling case. (a) Transmitted (orange) and reflected (blue) trajectories with force arrows from the complex-extended Eckart potential surface. The center of the pole in this potential is denoted by the red dot. The trajectories follow classical paths through the complex coordinate space. (b) Kinetic energy profile for the transmitted trajectory in part a. An orange box denotes the region where the real component of the kinetic energy is negative.

problems. It is seen that in the regions of interest (near the isochrones) the resultant initial velocity vector is directed toward positive x. Overlaying Figures 9 and 10 can help one define where isochrones might be located, as one can obtain an idea of the initial impetus each trajectory will have and what forces will influence its subsequent evolution. In addtion, as seen in eq 44, trajectories located to the left of the center of the initial wave packet (for CVDPM(3) and CVDPM(4) trajectories) will have v_{iniital} that contains a component in the negative y direction.

It is interesting to trace the transmitted trajectory's path through this force field knowing that the initial impetus is in the positive x direction. The transmitted trajectory shows a large slowdown in the x direction as the trajectory begins to decelerate in the barrier region. While the trajectory is decelerating in the x direction, it very quickly accelerates in the y direction. This trajectory is able to circumvent the pole located near $z = -0.35\mathrm{i}$ by slipping around the top. The reflected trajectory, however, is not able to do the same. It encounters very large forces repelling it away from the barrier region, and subsequently this trajectory reaches a turning point in the x direction and reverses course. In essence, the pole plays a role similar to that of the nucleus in the Rutherford foil experiment—some trajectories are able to skirt above or below the pole (which, of course, will affect the trajectory's arrival time), while some trajectories will aim right for the pole and will subsequently be back-scattered into the reflected region.

Figure 9b shows the transmitted trajectory from Figure 9a by plotting both the real and the imaginary parts of the kinetic energy versus the propagation time on the z-axis. Note that as the trajectory enters the barrier region ($t \approx 0.25$) there is a decrease in the real kinetic energy and a corresponding increase in the imaginary kinetic energy (features that can also be seen in Figure 9a). The real kinetic energy can even be seen to go negative for 0.75 a.u. To help understand this, we will decompose the complex-valued kinetic energy into real and imaginary parts

$$\mathrm{KE} = \frac{(p_x + \mathrm{i}p_y)^2}{2m} = \frac{{p_x}^2 - {p_y}^2}{2m} + \mathrm{i}\,\frac{p_x p_y}{m} \qquad (45)$$

The real component of the kinetic energy can take on negative values if $|p_x| < |p_y|$. However, from Figure 9b, when the real component of the kinetic energy is negative, the imaginary component of the kinetic energy is positive, indicating that p_x and p_y are either both positive or negative values. Figure 9a reveals that the trajectory is moving in the positive y direction at this time, thus showing that even when the real kinetic energy is negative the trajectory is still making progress in the direction of the positive real axis.

4.4. Quantum Complex Trajectories. Figure 11 shows trajectories for the HE Gaussian scattering problem as well as a contour map for the complex-extended Gaussian potential. The solid red lines indicate third-order trajectories originating to the left of the wave packet center that cross the real axis twice. CVDPM(3) trajectories originating on the right of the wave packet center only exhibit one crossing of the real axis. CVDPM(3) trajectories originating to the left of the wave packet center will cross the real axis once at a time (around $t = 0.7$) prior to the specified arrival time $t_{\mathrm{a}} = 1.5$, then cross the real axis once more at the specified arrival time. These trajectories are repelled by a very strong potential energy wall once they cross the real axis at $t = 0.7$. This imparts a force in the negative y direction that induces the second crossing. At both of these crossing points, the trajectory exhibits a probability density that matches the exact value of the density at that time and at that point in space as determined by the grid calculation. Carrying the integration to later times reveals that these trajectories will not cross the real axis again, at a time greater than $t_{\mathrm{a}} = 1.5$, as there will be no force component to impart an upward motion to the trajectory (it has already moved beyond the barrier region). This figure also shows a second-order trajectory that is launched from an identical position as one of the transmitted third-order trajectories. Note that it does not approach close to the real axis on the time scales of interest.

Figure 12a shows the real and imaginary parts of the wave function plotted against U_{I} (the imaginary part of the potential) and the probability density for the CVDPM(2) trajectory plotted in Figure 11. Figure 12b shows the same, only plotted this time for the CVDPM(3) trajectory launched with the same initial conditions as the CVDPM(2) trajectory. Figure 11 showed that both the CVDPM(3) and the CVDPM(2) trajectories will transmit the barrier ($x > 0$), but the CVDPM(2) trajectory will not be detected because there is no time at which $y = 0$. In the Appendix it is shown that the real and imaginary parts of $A(z,t)$ in the CVDPM(n) equations can be expressed in a form that is similar to the of RVDPM(n) equations, albeit complex-valued. The density can be computed at any point through the relation $\rho(z,t) = \exp(-2/\hbar\ \mathrm{Im}(A(z,t)))$. The time derivative of the

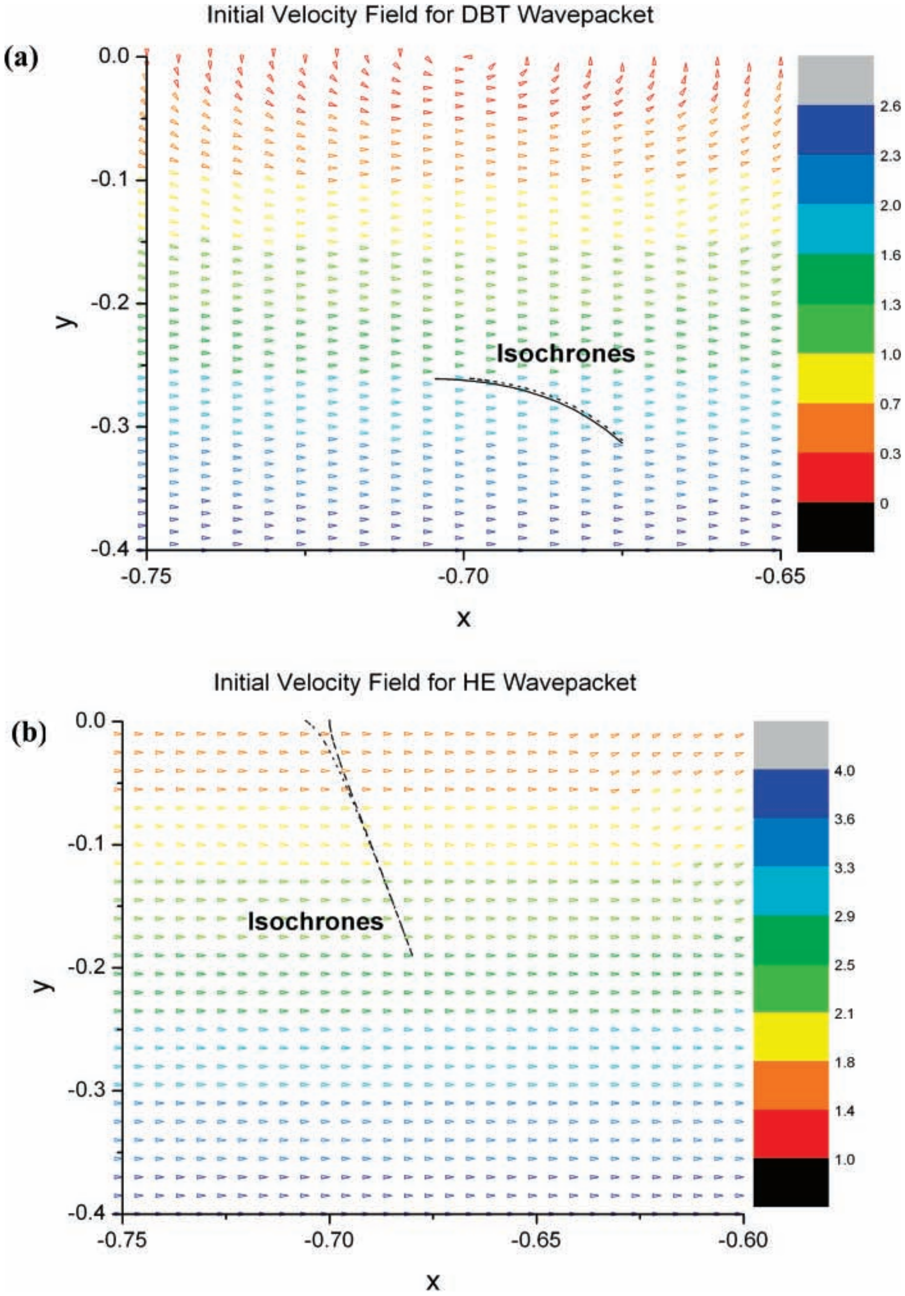

Figure 10. Initial velocity fields, colored by magnitude, with CVDPM(2) (dashed) and CVDPM(3) (solid) isochrones: (a) deep tunneling problem; (b) high-energy scattering problem.

imaginary component $A(z,t)$ (given in the Appendix as $G(z,t)$), containing density information, is given by

$$\frac{dG(z,t)}{dt} = \frac{\hbar}{2m} F_2 - U_I \tag{46}$$

while the time derivative of the real component of $A(z,t)$, the phase of the wave function, is given by

$$\frac{dF(z,t)}{dt} = \frac{1}{2m} F_1^{\ 2} - U_R - \frac{\hbar}{2m} G_2 + \frac{1}{2m} G_1^{\ 2} \tag{47}$$

Substituting eq 46 into the expression for $\rho(z,t)$ yields

$$\rho(z,t) = \exp\left(-\frac{1}{m}\int_0^t F_2 \, dt + \frac{2}{\hbar}\int_0^t U_I \, dt\right) \tag{48}$$

Figure 12a illustrates how the real and imaginary parts of the wave function as well as $\rho(z,t)$ vary with position versus the variation in U_I.

It is important to note the behavior of U_I in Figures 12a and 12b. The two trajectories start with the same initial position and for early times U_I are similar for both trajectories. A difference develops, however, in Figure 12a, around $x \approx 0.5$ a.u. It is noted that U_I changes sign and becomes a positive-valued function that decays to zero when $x > 1$ (away from the barrier region). It is around this point that $\rho(z,t)$ stops declining and starts to increase. The density computed along this trajectory remains large and does not decay to the correct value by $t_a = 1.5$. In Figure 12b, however, $\rho(z,t)$ is seen to decay to the value found on the real axis at $t = 1.5$. The behavior of $\rho(z,t)$ with respect to that of U_I can be examined with eq 48. If U_I is positive, then it is serving to increase the value of $\rho(z,t)$, while

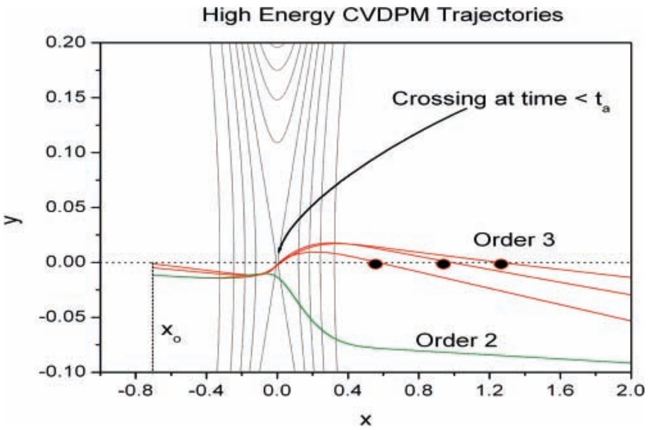

Figure 11. CVDPM(n) trajectories for the HE Gaussian scattering problem, with contours of the absolute value of the complex-extended Gaussian potential. The red lines represent CVDPM(3) trajectories that exhibit two crossings with the real axis and originate on the left side of the center of the wave packet. The green line is a CVDPM(2) trajectory launched from the same initial position as one of the third-order trajectories.

the opposite is true for a negative value for U_I, as seen in Figure 12b. The path of the trajectory through the complex plane must be chosen such that the integral of U_I cancels just enough of the integral of F_2 (in eq 46) such that the correct density is transported by the trajectory when it crosses the real axis at the arrival time. It is shown in the Appendix that eq 46 reduces to eq 9 on the real axis. The complex-extended potential is seen to have a dual role for the CVDPM(n) trajectories. As in RVDPM(n), the real component of the potential still determines the motion of the trajectory in the x direction. Likewise, the imaginary component of the potential will determine the motion of the trajectory in the y direction.

5. Conclusions

Given the appropriate order, RVDPM(n) was shown to be a quick method for obtaining a very good approximation to transmission probabilities in barrier scattering problems, including the deep tunneling case. Because there are no functional fittings and very few trajectories are required to evaluate the bifurcation point, RVDPM(n) yields vast computational savings over other quantum trajectory methods. RVDPM(n) trajectories are parallelizable, and RVDPM(n) trajectory results have been presented for three-dimensional problems.[35] There are several known problems with RVDPM(n), however. High orders of RVDPM(n) are required in regions where the wave function develops nodes or in regions of interference. Additionally, the results may not be very good. In problems where the barrier is thin compared to the width of the initial wave packet, the transmitted wave function may not be very accurate. Presently, there is no way of predicting the best order of RVDPM(n) to use for a particular barrier scattering problem, though in general it seems that results for higher-energy problems are very good with low orders of DPM while deep tunneling problems require higher orders to produce good transmission probabilities.

CVDPM(n) trajectories very accurately reproduce transmission probabilities at low orders in both the deep barrier tunneling and the higher-energy barrier scattering problems for thick barriers. For both the Eckart and the Gaussian potentials it was found that CVDPM(3) was sufficient to almost exactly predict the transmission probability for deep barrier tunneling problems while CVDPM(2) was sufficient for high-energy scattering problems. CVDPM(n) demonstrates good convergence properties on the potential energy surfaces (Eckart and Gaussian) under study. However, it is not to be expected that this will be true for every potential energy surface of interest—more study is needed in this area. Because CVDPM(n) is just the DPM applied to the complex-extended quantum Hamilton−Jacobi equations, CVDPM(n) trajectories will also share the same parallizability as their RVDPM(n) counterparts. Again, very few CVDPM(n) trajectories are needed to accurately compute the transmission probability, and we have recently extended this method to two-dimensional[65] (one translational and one vibrational) barrier transmission problems.

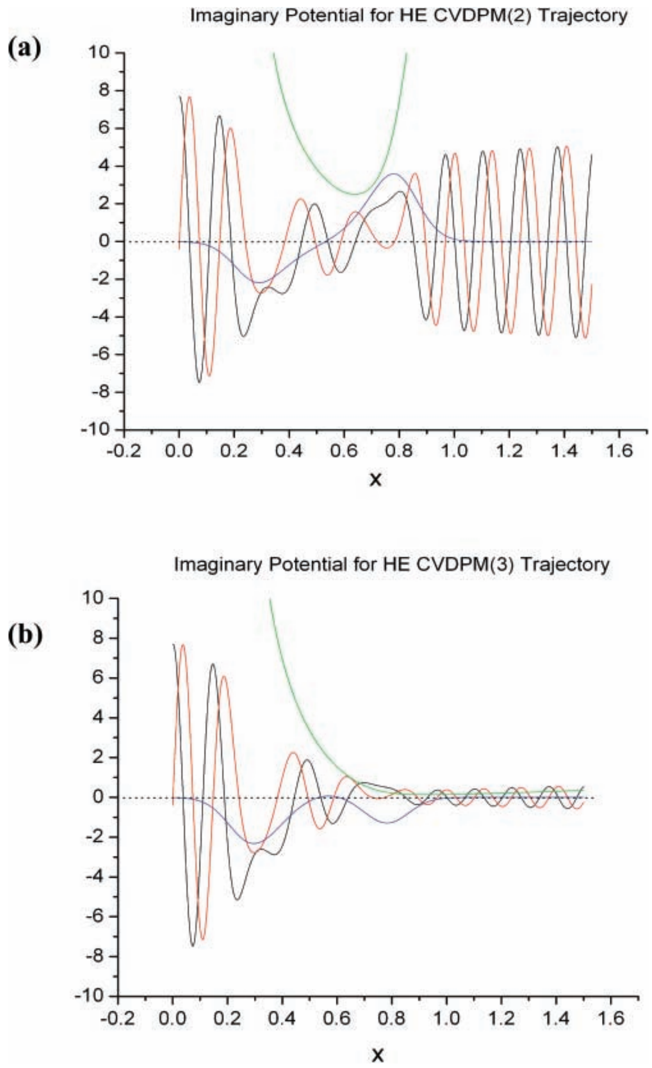

Figure 12. Imaginary potential U_I (blue) with real (black) and imaginary (red) parts of the wave function and density (green). (a) CVDPM(2) trajectory for the HE Guassian barrier scattering problem. The sign of U_I determines the behavior of the density. A positive U_I leads to a growing density while a negative U_I forces the density to decay. (b) CVDPM(3) trajectory. Note how the initial value of the wave function gradually decreases to the expected value at the arrival time t_a.

In all, the greatest difficulty with CVDPM(n) lies in locating the isochrones from which one obtains the initial spatial coordinates needed to launch the trajectories. In two dimensions, this situation becomes worse, as the isochone will become a surface in four-dimensional space,[65] and consequently this makes location of the initial coordinates much more difficult. Higher-dimensional problems will introduce even more difficulty into the isochrone location problem. Also, computation of the transmission probability at intermediate time steps requires searching for the location of new isochrones. Depending upon the situation, one may lose much of the computational advantage in CVDPM(*n*) through the isochrone location problem. Another possible problem with CVDPM(*n*) concerns potentials that do not have a global analytical function by which to perform the analytic continuation (ab initio potentials, for example). This directly impacts situations that will be of interest to the quantum dynamicist. However, there are methods for numerically constructing the analytic continuation of a function given only discrete data on the real axis, and this problem may prove tractable. In spite of these issues, CVDPM(*n*) still proves to be a very interesting method for computing transmission probabilities.

Further studies are in progress concerning the behavior of CVDPM(*n*) trajectories in thick *v*, thin barrier scattering problems, as well as more detailed analysis of isochrones.[66] Anticipated extensions of CVDPM(*n*) include collinear reactive scattering and extension of Wigner trajectories to barrier scattering problems in complex phase space as well as further generalization of the method to make it applicable to a wider range of barrier scattering (even multidimensional) problems. It is hoped that further examination of the behavior of complex quantum trajectories will lead to robust and accurate methods for quickly computing transmission probabilities in quantum mechanical barrier scattering problems.

Appendix: Correspondence Between RVDPM(*n*) and CVDPM(*n*)

In this appendix, correspondence between the equations of motion for RVDPM(*n*) and CVDPM(*n*) trajectories will be explored. The guiding principle is that, on the real axis, the equations for CVDPM(*n*) should be identical to the equations provided by RVDPM(*n*). Equations 1 and 25 describe the same wave function on the real axis; hence, the arguments in the exponents should be equal

$$C(x,t) + \frac{i}{\hbar} S(x,t) = \frac{i}{h} A(x,t) \tag{A1}$$

The complex action $A(x,t)$ can be decomposed into real and imaginary parts

$$A(z,t) = F(z,t) + iG(z,t) \tag{A2}$$

Subsituting eq A2 into eq A1 yields the following equations relating the real-valued $C(x,t)$ and $S(x,t)$ functions to their CVDPM(*n*) counterparts on the real axis

$$F(x,t) = S(x,t) \tag{A3}$$

and

$$G(x,t) = -\hbar C(x,t) \tag{A4}$$

Equations A3 and A4 are worth noting. They show that real component of the complex-valued $A(z,t)$ can be identified with the $S(x,t)$ function from RVDPM(*n*). The imaginary component of $A(z,t)$ is seen to be proportional to the *C*-amplitude in RVDPM(*n*). Note, however, that these relationships are valid only on the real axis.

Substituting equation A2 into eq 26 and decomposing the analytically extended potential *U* into real and imaginary parts $U(z) = U_R(z) + iU_I(z)$, where U_R, U_I are real-valued functions, give

$$F_t + iG_t = -U_R - \frac{1}{2m}(F_1^{\,2} + 2iF_1G_1 - G_1^{\,2}) + \frac{i\hbar}{2m}(F_2 + iG_2) - iU_I \tag{A5}$$

where all derivatives are taken with respect to the complex coordinate *z*. Separating eq A5 into real and imaginary parts and substituting eqs A3 and A4 yield two coupled equations

$$\frac{\partial F(z,t)}{\partial t} = -\frac{1}{2m} F_1^{\,2} - U_R - \frac{\hbar}{2m} G_2 + \frac{1}{2m} G_1^{\,2} \tag{A6}$$

and

$$\frac{\partial G(z,t)}{\partial t} = -\frac{1}{2m}[-\hbar F_2 + 2F_1G_1] - U_I \tag{A7}$$

These equations can be transformed into the Lagrangian frame through the use of eq 6. These transformed equations become

$$\frac{dF(z,t)}{dt} = \frac{1}{2m} F_1^{\,2} - U_R - \frac{\hbar}{2m} G_2 + \frac{1}{2m} G_1^{\,2} \tag{A8}$$

and

$$\frac{dG(z,t)}{dt} = \frac{\hbar}{2m} F_2 - U_I \tag{A9}$$

To make progress, the behavior of eqs A6−A9 on the real axis must be examined. On the real axis, $U_I = 0$, and U_R will be equal to *V*, the real-valued potential. Employing eqs A3 and A4 in eqs A6−A9 will generate the appropriate equations on the real axis. This is seen to make the Eulerian equations for *S*, eqs A6 and 2, equivalent. Likewise, eqs A7 and 4 will also be equal. The Lagrangian equations A8 and A9 are also shown to yield the RVDPM(*n*) equations on the real axis.

A similar analysis can be carried through for the first two orders of CVDPM. Eulerian equations for S_1 and C_1 can be derived from the CVDPM(1) equation, eq 30, in the same manner as outlined above. Again, two coupled equations are obtained, which have the form

$$\frac{\partial F_1}{\partial t} = -\frac{1}{m} F_1F_2 - U_{R,1} - \frac{\hbar}{2m} G_3 + \frac{1}{m} G_1G_2 \tag{A10}$$

and

$$\frac{\partial G_1}{\partial t} = -\frac{1}{2m}[-\hbar F_3 + 2F_2G_1 + 2F_1G_2] - U_{I,1} \tag{A11}$$

Lagrangian versions of eqs A10 and A11 are

$$\frac{dF_1}{dt} = -U_{R,1} - \frac{\hbar}{2m} G_3 + \frac{1}{m} G_1G_2 \tag{A12}$$

and

$$\frac{dG_1}{dt} = -\frac{1}{2m}[-\hbar F_3 + 2F_2G_1] - U_{I,1} \tag{A13}$$

Evaluating the equations on the real axis generates equations (both Eulerian and Lagrangian) that are equivalent to the RVDPM(2) equations.

An analysis of CVDPM(2) equations shows the same trend repeating, and one can derive Lagrangian equations for any order of CVDPM(*n*) by using the following equations

$$\frac{\mathrm{d}G_n}{\mathrm{d}t} = -\frac{1}{2m}[-\hbar F_{2+n} + 2(G_1F_1)_n] + \frac{1}{m}F_nG_{1+n} - U_{\mathrm{I},n} \qquad \text{(A14)}$$

and

$$\frac{\mathrm{d}F_n}{\mathrm{d}t} = -\frac{1}{2m}(F_1^{\ 2})_n + \frac{1}{2m}[-\hbar G_{2+n} + (G_1^{\ 2})_n] - U_{\mathrm{R},n} + \frac{1}{m}F_1F_{1+n} \qquad \text{(A15)}$$

As for CVDPM(0) and CVDPM(1), the only difference between RVDPM(n) equations and the equations derived from CVDPM(n) is the term of the form $U_{\mathrm{I},n}/\hbar$ appearing in the C_n equations and the replacement of V_n by $U_{\mathrm{R},n}$ in the S_n equations. Equations A14 and A15 reduce to eqs 18 and 19, respectively, on the real axis. Thus, all equations of CVDPM(n) correspond to those of RVDPM(n) on the real axis, as required.

Acknowledgment. We thank Chia-Chun Chou and Julianne David for helpful discussions as well as the Welch Foundation of Houston, Texas, for support of this work.

References and Notes

(1) Zhang, J. Z. H. *Theory and Application of Quantum Molecular Dynamics*; World Scientific: River Edge, NJ, 1999.

(2) Wyatt, R. E. *Quantum Dynamics with Trajectories: Introduction to Quantum Hydrodynamics*; Springer: New York, 2005.

(3) Bohm, D. *Phys. Rev.* **1952**, *85*, 166.

(4) Bohm, D. *Phys. Rev.* **1952**, *85*, 180.

(5) Madelung, E. *Z. Phys.* **1926**, *40*, 322.

(6) de Broglie, L. *J. Phys.* **1927**, *8*, 225.

(7) Holland, P. R. *The Quantum Theory of Motion: An Account of the de Broglie−Bohm Causal Interpretation of Quantum Mechanics*; Cambridge University Press: New York, 1993.

(8) Holland, P. *Ann. Phys.* **2005**, *315*, 505.

(9) Takabayasi. T. *Prog. Theor. Phys.* **1954**, *11*, 341.

(10) Burghardt, I.; Cederbaum, L. S. *J. Chem. Phys.* **2001**, *115*, 10303.

(11) Burghardt, I.; Cederbaum, L. S. *J. Chem. Phys.* **2001**, *115*, 10312.

(12) Burghardt, I.; Moller, K. B.; Parlant, G.; Cederbaum, L. S.; Bittner, E. R. *Int. J. Quantum Chem.* **2004**, *100*, 1153.

(13) Lopreore, C. L.; Wyatt, R. E. *Phys. Rev. Lett.* **1999**, *82*, 5190.

(14) Wyatt, R. E. *J. Chem. Phys.* **1999**, *111*, 4406.

(15) Babyuk, D.; Wyatt, R. E. *Chem. Phys. Lett.* **2004**, *400*, 145.

(16) Babyuk, D.; Wyatt, R. E. *J. Chem. Phys.* **2004**, *121*, 9230.

(17) Wyatt, R. E.; Babyuk, D. *Phys. Rev. E* **2006**, *73*, 10.

(18) Babyuk, D.; Wyatt, R. E. *J. Chem. Phys.* **2006**, *124*, 7.

(19) Babyuk, D.; Wyatt, R. E. *J. Chem. Phys.* **2006**, *125*, 7.

(20) Kendrick, B. K. *J. Chem. Phys.* **2003**, *119*, 5805.

(21) Pauler, D. K.; Kendrick, B. K. *J. Chem. Phys.* **2004**, *120*, 603.

(22) Kendrick, B. K. *J. Chem. Phys.* **2004**, *121*, 2471.

(23) Poirier, B. *J. Chem. Phys.* **2004**, *121*, 4501.

(24) Trahan, C.; Poirier, B. *J. Chem. Phys.* **2006**, *124*, 14.

(25) Trahan, C.; Poirier, B. *J. Chem. Phys.* **2006**, *124*, 18.

(26) Rassolov, V. A.; Garashchuk, S. *J. Chem. Phys.* **2004**, *120*, 6815.

(27) Garashchuk, S.; Rassolov, V. A. *J. Chem. Phys.* **2004**, *121*, 8711.

(28) Rassolov, V. A.; Garashchuk, S. *Phys. Rev. A* **2005**, *71*, 10.

(29) Trahan, C. J.; Hughes, K.; Wyatt, R. E. *J. Chem. Phys.* **2003**, *118*, 9911.

(30) Trahan, C. J.; Wyatt, R. E. *J. Chem. Phys.* **2003**, *119*, 7017.

(31) Trahan, C. J.; Wyatt, R. E. *Chem. Phys. Lett.* **2004**, *385*, 280.

(32) Hughes, K. H.; Wyatt, R. E. *J. Chem. Phys.* **2004**, *120*, 4089.

(33) Hughes, K. H. *J. Chem. Phys.* **2005**, *122*, 11.

(34) Bittner, E. R. *J. Chem. Phys.* **2003**, *119*, 1358.

(35) Trahan, C. J.; Wyatt, R. E.; Poirier, B. *J. Chem. Phys.* **2005**, *122*, 9.

(36) John, M. V. *Found. Phys. Lett.* **2002**, *15*, 329.

(37) Yang, C. D. *Ann. Phys.* **2005**, *319*, 399.

(38) Yang, C. D. *Chaos, Solitons Fractals* **2006**, *30*, 41.

(39) Yang, C. D. *Chaos, Solitons Fractals* **2006**, *30*, 342.

(40) Yang, C. D. *Chaos, Solitons Fractals* **2007**, *32*, 312.

(41) Chou, C. C.; Wyatt, R. E. *J. Chem. Phys.* **2006**, *125*, 10.

(42) Chou, C. C.; Wyatt, R. E. *Phys. Rev. E* **2006**, *74*, 9.

(43) Chou, C. C.; Wyatt, R. E. *Int. J. Quantum Chem.*, in press.

(44) Boiron, M.; Lombardi, M. *J. Chem. Phys.* **1998**, *108*, 3431.

(45) Goldfarb, Y.; Degani, I.; Tannor, D. J. *J. Chem. Phys.* **2006**, *125*, 4.

(46) Heller, E. *J. Chem. Phys.* **1975**, *62*, 1544.

(47) Shalashilin, D.; Child, M. *J. Chem. Phys.* **2000**, *113*, 10028.

(48) Shalashilin, D.; Child, M. *J. Chem. Phys.* **2001**, *114*, 9296.

(49) Shalashilin, D.; Child, M. *J. Chem. Phys.* **2001**, *115*, 5367.

(50) Martinez, T.; Ben-Nun, M.; Levine, R. *J. Phys. Chem.* **1996**, *100*, 7884.

(51) Ben-Nun, M.; Martinez, T. *J. Chem. Phys.* **1998**, *108*, 7244.

(52) Ben-Nun, M.; Martinez, T. *J. Phys. Chem.* **2000**, *112*, 6113.

(53) Swada, S.; Heather, R.; Jackson, B.; Metiu, H. *J. Chem. Phys.* **1985**, *83*, 3009.

(54) Garashchuk, S.; Rassolov, V. A. *Chem. Phys. Lett.* **2002**, *364*, 562.

(55) Cook, D. B. *Probability and Schrödinger's Mechanics*; World Scientific: River Edge, NJ, 2002.

(56) Tannor, D. J. *Introduction to Quantum Mechanics: A Time-Dependent Perspective*; University Science Books: Sausalito, CA, 2007.

(57) Huber, D.; Heller, E. J. *J. Chem. Phys.* **1987**, *87*, 5302.

(58) Huber, D.; Heller, E. J.; Littlejohn, R. G. *J. Chem. Phys.* **1988**, *89*, 2003.

(59) de Aguiar, M. A. M.; Baranger, M.; Jaubert, L.; Parisio, F.; Ribeiro, A. D. *J. Phys. A: Math. Gen.* **2005**, *38*, 4645.

(60) Rowland, B. A.; Wyatt, R. E. *Chem. Phys. Lett.* **2006**, *426*, 209.

(61) Arfken, G. B.; Weber, H.-J. *Mathematical Methods for Physicists*, 5th ed.; Harcourt/Academic Press: San Diego, CA, 2001.

(62) Kwok, Y. K. *Applied Complex Variables for Scientists and Engineers*; Cambridge University Press: New York, 2002.

(63) Holmes, M. H. *Introduction to Numerical Methods in Differential Equations*; Springer: New York, 2007.

(64) Hundsdorfer, W. H.; Verwer, J. G. *Numerical Solution of Time-Dependent Advection−Diffusion−Reaction Equations*; Springer: New York, 2003.

(65) Wyatt, R. E.; Rowland, B. A. *J. Chem. Phys.* in press.

(66) David, J. K.; Wyatt R. E., to be submitted for publication.